Published in IEEE Antennas and Wireless Propagation Letters,
vol.13, pp.682,685, 2014

A Comparison of the Performance of THz Photoconductive Antennas

E. Moreno, M. F. Pantoja, *Senior Member, IEEE*, A. R. Bretones, *Senior Member, IEEE*, M. Ruiz-Cabello, and S. G. Garcia, *Member, IEEE*

***Abstract*—This letter explores the influence of the geometry of bias electrodes in the performance of terahertz (THz) photoconductive antennas (PCAs). To this end, a methodology is presented to calculate numerically the operational bandwidth and radiation efficiency of the PCAs. The procedure is validated through a comparison to experimental measurements. Also, results are depicted from numerical simulations of different PCAs under varying conditions of bias voltage, doping factor, and incident optical power. It is concluded that an appropriate configuration of the electrodes may double the efficiency of the antennas, with a penalty in the bandwidth of the radiated pulse usually smaller than 10%.**

***Index Terms*—Photoconductive antennas, terahertz technology.**

I. Introduction

TERAHERTZ (THz) technology has become one of the most active research fields in recent years [1]. The unique properties of the interaction of THz electromagnetic waves with matter have allowed us to foresee outstanding applications in spectroscopy, such as detection of chemical materials, biological agents, or early-stage damages in carbon-fiber materials [2]. However, the high attenuation of THz waves in ambient air is a major drawback that is usually addressed by the more expensive high-power sources [3]. As a consequence, the economic cost of the commercial models still remains unaffordable for most small research laboratories, and some efforts have been oriented toward the development of low-profile THz sources, such as the photoconductive antennas (PCAs) [4].

Based on the Auston switch [5], the typical operating frequencies of PCAs are in the 1–5 THz range, reported configurations being able to radiate up to 60 THz by employing substrates composed of semiconductors with low recombination time of carriers [6]. However, the reported optical-to-THz conversion efficiency is also low, ranging from 0.01% to 0.1% for average optical powers of 1–50 mW [7]. Practical applications of PCAs have used different combinations of substrates, electrodes, bias voltages, and incident optical powers, reporting different efficiencies for each case [8], [9]. In this line of research, the exploration of possibilities through appropriate computer-aided design (CAD) techniques to achieve a better performance of PCAs is a step forward, and this constitutes the main objective of this letter.

To this end, several geometries of bias electrodes over a LT-GaAs substrate are initially taken into account [10], [11], and the Auston switch configuration is explored under varying conditions of the doping of the semiconductor, the bias voltage, and the optical pump power. The numerical results are based on a full-wave finite-difference time-domain (FDTD) solver for drift-diffusion and Maxwell's equations [12], which outperforms the accuracy of other semi-analytical CAD techniques [7] at a cost of higher computational demands. A validation of the code for our purposes is made with the experimental measurements presented in [8].

II. Efficiency of PCAs

Unlike microwave antennas, PCAs in the THz regime are fed with two different sources: an optical source, usually a femtosecond laser, which provides enough energy to allow carriers to flow to the conduction band; and a dc voltage source, which biases the semiconductor to drive any photogenerated carrier between electrodes. The resulting electric current acts as the source of THz electromagnetic fields, whose waveforms depend on several quantities such as the physical properties of the semiconductor, the geometry and bias voltage of the dc source, and the power and waveform of the impinging laser pulse. In this way, the calculation of the antenna efficiency requires the radiated and input energy, W_{rad} and W_{in} respectively, to be accounted for in the form

$$\eta = \frac{W_{\mathrm{rad}}}{W_{\mathrm{in}}} = \frac{W_{\mathrm{rad}}}{W_{\mathrm{DC}} + W_{\gamma}} \tag{1}$$

where W_{DC} is the energy provided by the dc source, and W_{γ} is the energy rendered by the laser source. For pulsed systems, (1) is equivalent to the usual definition of antenna efficiency in terms of radiated and input power [7].

Experimental setups employ laser sources of pulse duration σ_t, repetition rate ν_{γ}, and an average power $P_{\mathrm{opt,av}}$. The peak optical power can be derived as $P_{\mathrm{opt,peak}} = P_{\mathrm{opt,av}}\sigma_t^{-1}\nu_{\gamma}^{-1}$, and the peak optical intensity is $I_0 = P_{\mathrm{opt-peak}}\pi^{-1}\sigma_r^{-2}$, where σ_r is the beam waist radius on the vacuum-semiconductor interface. It is also assumed that the optical source circularly illuminates the semiconductor. Then, the distribution of the photogenerated carriers $G_{\gamma}(r,t)$ can be calculated as

$$G_{\gamma}(r,t) = I_0 e^{-((r-r_0)/\sigma_r)^2} e^{-((t-t_0)/\sigma_t)^2} \tag{2}$$

Manuscript received November 07, 2013; revised February 21, 2014; accepted March 26, 2014. Date of publication March 28, 2014; date of current version April 17, 2014. This work was supported in part by the Spanish Ministry of Education under Project CSD2008-00068, the Junta de Andalucia Project P09-TIC-5327, the EU FP7/2007-2013 under Grant 205294 (HIRF-SE project), and the Spanish National Project TEC2010-20841-C04-04. *(Corresponding author: M. F. Pantoja.)*

The authors are with the Department of Electromagnetism and Matter Physics, University of Granada, 18071 Granada, Spain (e-mail: emorenop@ugr.es; mario@ugr.es; arubio@ugr.es; mcabello@ugr.es; salva@ugr.es).

Color versions of one or more of the figures in this letter are available online at http://ieeexplore.ieee.org.

Digital Object Identifier 10.1109/LAWP.2014.2314260

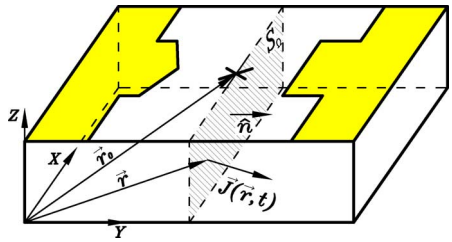

Fig. 1. Scheme of the central part of the electrodes and semiconductor in a typical PCA. The depicted inner surface is chosen to calculate the total current.

where r_0 is the center of the laser spot, and t_0 is the reference time. The optical energy is then calculated as

$$W_\gamma = \lim_{s\to+\infty} \int_0^{s\sigma_t} \int_0^{2\pi} \int_0^{s\sigma_r} G_\gamma(r,t) r dr d\varphi dt = \left(\sqrt{\pi}\right)^3 \sigma_r^2 \sigma_t I_0 = \sqrt{\pi}\sigma_t P_{\text{opt-peak}}. \quad (3)$$

Regarding the energy delivered by the dc source, the bias voltage V_{DC} remains constant in the radiation process, and the total electric current $I_{\text{DC}}(t)$ can be calculated by considering an inner surface S_0 between the electrodes of the semiconductor (Fig. 1). The numerical procedure is able to provide the local density of current $\vec{J}_{\text{DC}}(t)$ at the points located at S_0, and thus the power delivered by the dc source can be expressed as

$$P_{\text{DC}}(t) = V_{\text{DC}} I_{\text{DC}}(t) = V_{\text{DC}} \int_{S_0} \vec{J}_{\text{DC}}(t) \cdot d\vec{S} \quad (4)$$

and the energy delivered as

$$W_{\text{DC}} = \int_0^{\nu_\gamma^{-1}} P_{\text{DC}}(t) dt \quad (5)$$

where the integration time is limited to the pulse repetition time ν_γ^{-1}, because at that time the laser source is switched on again and a new electromagnetic pulse is generated. In this sense, it is worth remarking that (1) is calculated just considering only a single pulse of electromagnetic radiation. Identical results are achieved when a set of pulses is considered in the numerical simulator, which on the other hand is a usual procedure to decrease the noise in experimental setups.

Finally, the term in (1) corresponding to the radiated energy can be derived from the time-domain electric far fields $E_\theta(t)$ and $E_\varphi(t)$ by computing the total radiated power $P_{\text{rad}}(t)$

$$P_{\text{rad}}(t) = \frac{1}{\eta_0} \int_0^{2\pi} \int_0^{\pi} \left(|E_\theta(t)|^2 + |E_\varphi(t)|^2 \right) \sin(\theta) d\theta d\varphi \quad (6)$$

and then

$$W_{\text{rad}} = \int_0^{\nu_\gamma^{-1}} P_{\text{rad}}(t) dt. \quad (7)$$

Also, the corresponding average radiated power can be calculated as $P_{\text{rad,av}} = \nu_\gamma W_{\text{rad}}$.

III. Results

As indicated in Section I, the main objective of this letter is to compare the performance of PCAs by exploring different configurations of the device. Prior to this study [12], a validation of the numerical procedure was presented following the experimental setup of [8]. The inset of Fig. 2 shows the geometry of electrodes layered on a semiconductor substrate of LT-GaAs of thickness 1.5 μm, and a laser pulse impinges on the center of the electrodes ($\vec{r}_0$) where the electrostatic field is higher. Table I summarizes the numerical parameters of the laser pulse employed, as well as the characteristic constitutive parameters of the semiconductor substrate and the electrical description of carriers. Electrodes are assumed to behave as perfect electric conductors (PECs). Fig. 2 compares the experimental results of the average radiated power [8] for different incident laser pulses to those predicted by a numerical simulator, which is based on the FDTD solution of the coupled system of equations derived from the drift-diffusion model and Maxwell's equation [12], and the application of (6).

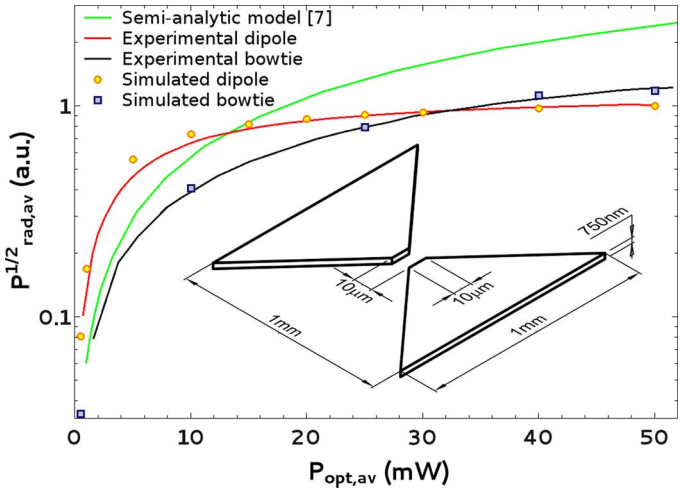

Fig. 2. Validation of the numerical procedure with [8] by: 1) experimental and full-wave simulation of the FF-dipole ($V_{\text{bias}} = 10$ V) depicted in Fig. 3; and 2) experimental, semi-analytic and full-wave simulations of the bow-tie dipole ($V_{\text{bias}} = 30$ V) shown in the inset.

TABLE I
Parameters Employed in the Simulations

LT-GaAs: parameters used in the simulation (T=300k)	
Auger recombination function parameters	
Electrons	Holes
$\tau_n = 0.3ps$	$\tau_p = 0.4ps$
$C_{An} = 7 \cdot 10^{-30} cm^6 s^{-1}$	$C_{Ap} = 7 \cdot 10^{-30} cm^6 s^{-1}$
$n_1 = 4.5 \cdot 10^6 cm^{-3}$	$p_1 = 4.5 \cdot 10^6 cm^{-3}$
Relative permittivity and permeability	
$\varepsilon_r = 13.26$ if $\omega < 6THz$ $\mu_r = 1.0$	
The laser and carriers generating rate function parameters	
Absorption coefficient 1.0 μm^{-1}	Transmittance 0.9999
Rate of pairs (e-h) 0.9999	$\lambda_\gamma = 780nm$
$\nu_\gamma = 80MHz$	$\sigma_r = 1.8\mu m$
$n_{GaAs}(\lambda_\gamma) = 3.83$	$\sigma_t = 80fs$
Spot radius 3 μm	

A. Numerical Exploration of PCAs

Performance of PCAs is affected mainly by: 1) the choice of the geometry of electrodes [10], [11], where the inner part of electrodes can be varied to achieve more intense electrostatic fields; 2) the power of the laser source [7], which is

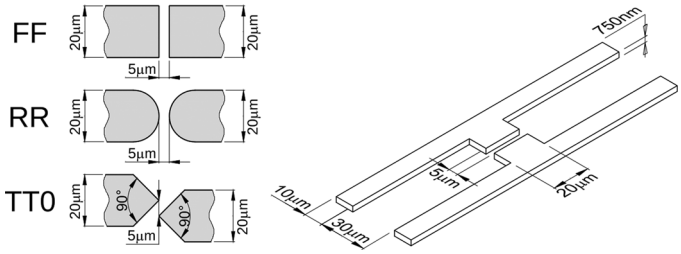

Fig. 3. Dimensions and geometries of *(left)* several configurations of electrodes, located at *(right)* the center of a PCA-dipole.

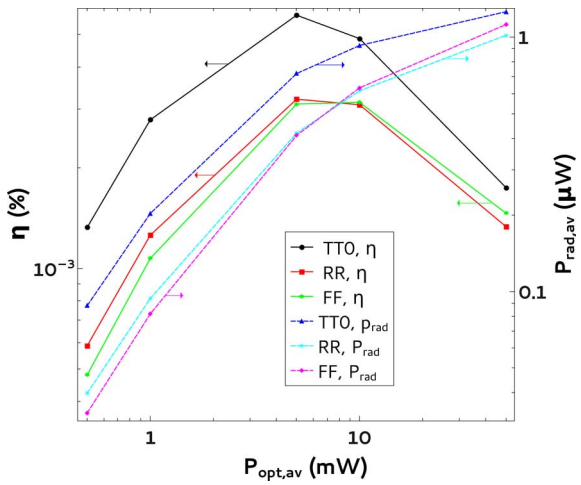

Fig. 4. Efficiency and radiated power for varying optical power. Net concentration charge and bias voltage are fixed at $5 \cdot 10^{16}$ cm^{-3} and 30 V, respectively.

usually increased to produce higher radiated power; 3) the bias voltage [8], [9], which is also increased to achieve the same effect of 2); and 4) the doping of the semiconductor [13], which strongly affects to the mobility of the carriers and thus the radiated electromagnetic field. This letter presents results for previously proposed choices of the: 1) geometry of electrodes, with rectangular (FF), rounded (RR), and triangular (TT0) forms (Fig. 3); 2) average laser power, ranging from 0.5 to 50 mW; 3) bias voltage, varying from 30 to 150 V; and 4) net concentration charge of $[-5{\cdot}10^{16}, 5{\cdot}10^{16}]$ cm^{-3}, thus including intrinsic, n-type, and p-type semiconductors. As figure-of-merit parameters, here we consider here the efficiency η, the average radiated power $P_{\mathrm{rad,av}}$, and, finally, the fractional bandwidth of the radiated pulse $\Delta f / f_{\max}$, where Δf corresponds to the half-power bandwidth of the radiated power.

Fig. 4 depicts the efficiency and radiated power as the optical power increases. For low values of $P_{\mathrm{opt,av}}$, the radiated power and the efficiency increase with an approximately linear dependence. However, for higher intensities of the laser pulse, there are more photogenerated carriers, and a screening effect appears near the electrodes by the accumulation of the majority carriers [7]. As a consequence, there is an inner field that opposes the incident field, and the radiated power reaches saturation for high values of $P_{\mathrm{opt,av}}$. The left vertical axis of Fig. 4 means efficiency, which becomes maximum near 5 mW and then decreases because there is a moderate increase in the radiated power, as can be inferred from (1). This effect is repeated for any simulated bias voltage and any net concentration charge.

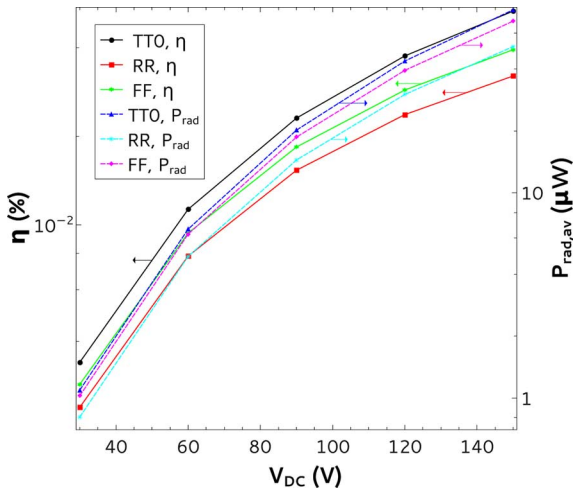

Fig. 5. Efficiency and radiated power for varying bias voltage. Net concentration charge and average optical power are fixed at $5 \cdot 10^{16}$ cm^{-3} and 20 mW, respectively.

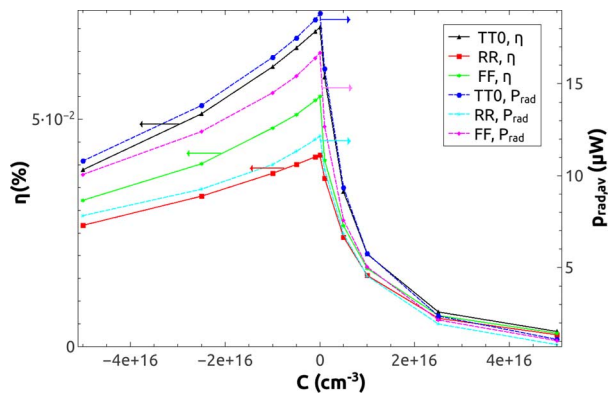

Fig. 6. Efficiency and radiated power for net concentration charges $C = N_D^+ - N_A^-$. Bias voltage and average optical power are fixed to 30 V and 20 mW, respectively.

A similar study is presented in Fig. 5 for the bias voltage. In this case, a linear effect for the radiated power is expected because of the drift of the carriers. However, in this case, a saturation effect is produced by: the mobility of the carriers, which is decreased by the bias field according to the Wien model [14]; the formerly explained capacitive effect of the accumulated carriers; and also the emitted radiation field, which reacts and decreases the effective bias field [15].

Regarding the dependence of the efficiency and the radiated power on the net concentration charge, Fig. 6 shows that $P_{\mathrm{rad,av}}$ for p-type semiconductors is higher than for n-type semiconductors. This is due to the higher mobility (μ_n) of n-type carriers, which create a higher space-charge polarization field and also produce a more intense screening effect of the external bias field [16]. For intrinsic semiconductors, the radiated power reaches a maximum because fewer carriers are involved, and the local polarization field is also lower. Similar reasoning can be used to explain the shape of the efficiency curves. Also in this case, the higher the net concentration charge, the higher the W_{DC}. This justifies the lower dynamic range of the efficiency curves for any geometry of electrodes.

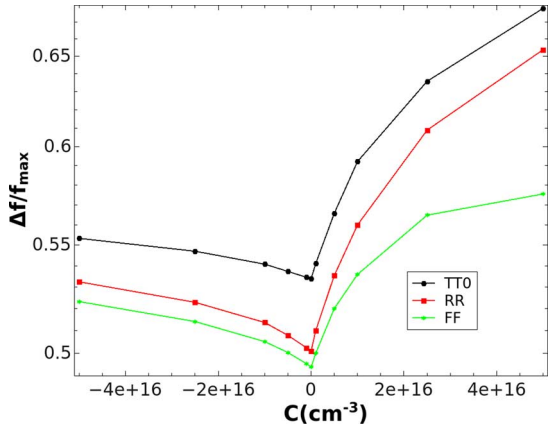

Fig. 7. Fractional bandwidth for varying net concentration charges.

Fig. 7 presents the fractional bandwidth for different net concentration charges. The asymmetric behavior for n and p semiconductors is explained in that the nonradiative recombination mechanisms for the decay of carriers depend on the minority carrier lifetime τ [17]. Thus, slower decay rates appear for n-type semiconductor ($\tau_p > \tau_n$), which implies a greater bandwidth of the electromagnetic radiation. It also bears remarking that Figs. 6 and 7 illustrate the limitation in the gain-bandwidth product for PCAs.

Finally, the influence of the geometry of the electrodes is analyzed. As reported in [10], conventional dipoles (FF) are outperformed by those with sharp features and offsets (TT0 dipole) or even with only offsets (RR dipole). For sharp features, the higher bias electric field results in higher total currents when compared to the rounded and planar geometries, and thus improvements are achieved in radiated power and efficiency. The main reason for the better performance of the RR dipole compared to the FF dipole is also given in [10]: The RR dipole has a bias electric field in both polarization directions, while the FF dipole enhances the optical power in only one direction. However, it bears noting that in Fig. 4, for higher optical power than 10 mW, the FF dipoles radiate strongly. This is due to the higher magnitude of the electric field at the lateral zone of the incident laser spot for the FF dipole, which compensates for the decrease of the cross-polar radiation.

IV. Conclusion

This letter has explored the performance of PCAs for varying parameters. Through a validated simulation procedure, it has been shown that a significant increase of the radiated power and efficiency can be achieved with the right choice of the geometry of the electrodes, incident optical power, and bias voltage. Further improvements in the bandwidth of the radiation can be achieved by doping the semiconductor. The presented simulations are in accordance with well-known theoretical concepts of carrier dynamics in semiconductors, which provides physical insight of the operating principles of PCAs.

References

[1] H.-J. Song and T. Nagatsuma, "Present and future of terahertz communications," *IEEE Trans. Terahertz Sci. Technol.*, vol. 1, no. 1, pp. 256–263, Sep. 2011.

[2] D. L. Woolard, R. Brown, M. Pepper, and M. Kemp, "Terahertz frequency sensing and imaging: A time of reckoning future applications?," *Proc. IEEE*, vol. 93, no. 10, pp. 1722–1743, Oct. 2005.

[3] H. Eisele, "State of the art and future of electronic sources at terahertz frequencies," *Electron. Lett.*, vol. 46, no. 26, pp. s8–s11, 2010.

[4] G. Chattopadhyay, "Technology, capabilities, and performance of low power terahertz sources," *IEEE Trans. Terahertz Sci. Technol.*, vol. 1, no. 1, pp. 33–53, Sep. 2011.

[5] D. H. Auston and M. C. Nuss, "Electrooptical generation and detection of femtosecond electrical transients," *IEEE J. Quantum Electron.*, vol. 24, no. 2, pp. 184–197, Feb. 1988.

[6] S. Kono, M. Tani, and K. Sakai, "Coherent detection of mid-infrared radiation up to 60 THz with an LT-GaAs photoconductive antenna," *IEE Proc., Optoelectron.*, vol. 149, no. 3, pp. 105–109, 2002.

[7] N. Khiabani, Y. Huang, Y. Shen, and S. Boyes, "Theoretical modeling of a photoconductive antenna in a terahertz pulsed system," *IEEE Trans. Antennas Propag.*, vol. 61, no. 4, pp. 1538–1546, Apr. 2013.

[8] M. Tani, S. Matsuura, K. Sakai, and S. i. Nakashima, "Emission characteristics of photoconductive antennas based on low-temperature-grown GaAs and semi-insulating GaAs," *Opt. Soc. Amer.*, vol. 36, pp. 7853–7859, 1997.

[9] L. Hou and W. Shi, "An LT-GaAs terahertz photoconductive antenna with high emission power, low noise, and good stability," *IEEE Trans. Electron Devices*, vol. 60, no. 5, pp. 1619–1624, May 2013.

[10] Y. Cai, I. Brener, J. Lopata, J. Wynn, L. Pfeiffer, and J. Federici, "Design and performance of singular electric field terahertz photoconducting antennas," *Appl. Phys. Lett.*, vol. 71, pp. 2076–2078, 1997.

[11] D. Li, Y. Huang, and Y.-C. Shen, "Analytical modelling of electric field in biased photoconductive antennas with advanced structure," in *Proc. Antennas Propag. Conf.*, Loughborough, U.K., 2008, pp. 241–244.

[12] E. Moreno, M. Pantoja, S. Garcia, J. Roldan, F. Ruiz, A. Bretones, and R. Martin, "On the simulation of carrier dynamics in terahertz photoconductive antennas," in *Proc. 7th EuCAP*, 2013, pp. 749–750.

[13] Y.-S. Lee, *Principles of Terahertz Science and Technology*, 1st ed. New York, NY, USA: Springer, 2009.

[14] T. Grasser and S. Selberherr, "MINIMOS-NT 2.1 Users Guide," Inst. Microelectron., TU Wien, Vienna, Austria, 2004.

[15] R. Ulbricht, E. Hendry, J. Shan, T. F. Heinz, and M. Bonn, "Carrier dynamics in semiconductors studied with time-resolved terahertz spectroscopy," *Rev. Modern Phys.*, vol. 83, no. 2, p. 543, 2011.

[16] P. U. Jepsen, R. Jacobsen, and S. Keiding, "Generation and detection of terahertz pulses from biased semiconductor antennas," *J. OSA B*, vol. 13, no. 11, pp. 2424–2436, 1996.

[17] B. G. Yacobi, *Semiconductor Materials: An Introduction to basic Principles*. Norwell, MA, USA: Kluwer, 2003.